Journal of Catalysis 371 (2019) 10–19

Contents lists available at ScienceDirect

Journal of Catalysis

journal homepage: www.elsevier.com/locate/jcat

Synergetic catalytic behavior of AgNi-OH-Pi nanostructures on Zr:$BiVO_4$ photoanode for improved stability and photoelectrochemical water splitting performance

Maged N. Shaddad, Prabhakarn Arunachalam *, Asma A. Alothman, Abeer M. Beagan, Matar N. Alshalwi, Abdullah M. Al-Mayouf *

Electrochemical Sciences Research Chair, Department of Chemistry, Science College, King Saud University, Riyadh, Saudi Arabia

ARTICLE INFO

Article history:
Received 3 September 2018
Revised 20 December 2018
Accepted 21 January 2019

Keywords:
Water splitting
Bismuth vanadate
Nickel hydroxylphosphate
Surface engineering

ABSTRACT

Photoelectrocatalytic methodologies are attractive for the longstanding storage of renewable energy via direct transformation of solar energy into fuels and chemicals. Controlled electrodeposition of thin and homogeneous nickel hydroxylphosphate (Ni-OH-Pi) nanoparticle films on Zr:$BiVO_4$ photoanodes was achieved, wherein the Ni-OH-Pi co-catalyst increased the photoelectrochemical (PEC) water oxidation and stability of photoanodes comprising silver phosphate (AgPi) on Zr:$BiVO_4$ (AgNi-OH-Pi/Zr:$BiVO_4$). Evaluation of the optical, structural, and morphological properties revealed that the AgNi-OH-Pi/Zr:$BiVO_4$ photoanodes exhibited enhanced PEC behavior with photocurrent densities (J_{ph}) of ~3.14 mA cm^{-2} for water oxidation with long-term stability over 60 h and ~4.15 mA cm^{-2} for hydrogen peroxide (0.5 M H_2O_2) oxidation. The enhanced PEC of the fabricated AgNi-OH-Pi/Zr:$BiVO_4$ photoanodes was attributed to the synergetic influence of strong visible-light absorption, enhanced charge separation–transport, and exceptional surface properties. Considering their comparatively superior photocatalytic activity, the AgNi-OH-Pi/Zr:$BiVO_4$ photoanodes are potential electrode candidates in solar water splitting, dye-sensitized solar cells, and photocatalysis.

1. Introduction

Visible-light-driven photoelectrochemical (PEC) water splitting (into hydrogen and oxygen) is a sustainable method for the production of clean and renewable fuels with a smaller carbon footprint; however, enhancing the water splitting efficiency is still challenging [1,2]. Notably, the efficiency of PEC water splitting is restricted by recombination of the photoinduced charges, which curtails commercialization of the technology due to the associated higher overpotentials, and the sluggish kinetics of water oxidation reactions on the membrane surface. From a techno-economical viewpoint, to achieve a cost effectiveness, the following features are required: (i) 10% solar-to-hydrogen (STH) efficiency, (ii) 1000 h long-term stability, and (iii) a targeted threshold cost of USD 2–4 per kg for distributed H_2 [3]. To fulfill these requirements, using earth abundant elements and lowering the cost of synthetic routes are imperative for the manufacture of PEC devices.

Semiconductors based on metal oxides, namely TiO_2 [4], Fe_2O_3 [5,6], WO_3 [7,8], and $BiVO_4$ [9–14], have been widely examined as candidate photoelectrode materials for advancement of the technology, as they are usually less readily oxidized than water. Among these, the n-type $BiVO_4$ semiconductor evokes considerable interest for employ in water-splitting PEC cells because it has a relatively small optical bandgap ~2.4 eV in the monoclinic phase and its CB edge is positioned close to 0 V vs. RHE [15]. Theoretically, $BiVO_4$ photoanodes can produce a maximal AM 1.5 photocurrent density of 7.5 mA cm^{-2} and absorb photons with energies higher than the band-gap, resulting in an STH energy conversion efficiency of 9% [16]. Besides, the absorption intensity of bare $BiVO_4$ photoanodes is very poor in the visible-light region, resulting in lower photocatalytic performance and AM 1.5 photocurrent density of <1 mA cm^{-2}. It is essential to apply a high voltage to attain a fairly high conversion efficiency, which may be owing to high

Abbreviations: CB, conduction band; PEC, photoelectrochemical; PBS, phosphate buffer solution; VB, valence band; WOCs, water oxidation catalysts.

* Corresponding authors.
E-mail addresses: parunachalam@ksu.edu.sa (P. Arunachalam), amayouf@ksu.edu.sa (A.M. Al-Mayouf).

https://doi.org/10.1016/j.jcat.2019.01.024
0021-9517/

surface recombination of the photoinduced hole/electron pairs. The use of bare $BiVO_4$ photoanodes in PEC water oxidation is strictly hampered due to its unsuitable CB energy level, shorter carrier lifetimes, and sluggish oxygen evolution kinetics [17]. Thus, a more efficient method must involve the use of catalytic/passivation layers on the $BiVO_4$ photoelectrode to suppress the surface recombination losses at the interface. In order to overcome the latter, water oxidation catalysts (WOCs) have been built on hole transfer catalysts such as CoPi and NiFeOx [10,16,18–22]. In particular, recently Zachäus et al. evidences that the photocurrent of $BiVO_4$ is restricted by surface recombination instead of charge transfer [23].

Thus, during the past decades, immense research efforts have been directed toward up-scalable WOCs. In this context, metal phosphates, such as cobalt phosphate and silver phosphate (AgPi), have generally been examined as electrode candidates for electrochemical and PEC applications. In particular, AgPi semiconductors have an indirect bandgap of 2.45 eV and are able to oxidize H_2O, suggesting that they can serve as promising hole transfer catalysts for visible-light-driven water oxidation [24,25]. Moreover, AgPi has photo-induced holes with strong oxidation abilities in the VB, and the mobility of the electron is considerably larger than that of the hole. This assists separation of the e^-/h^+ pairs, partially owing to the generation of delocalized π^* antibonding states in the CB. Moreover, the inductive nature of PO_4^{3-} assists charge separation, which effects in exceptional photocatalytic performance [26]. In this regard, Yi et al. applied AgPi as a functional material for photochemical water oxidation with the support of a sacrificial agent [27]. Menezes et al. recently demonstrated non-sacrificial water oxidation with AgPi nanoparticles in PBS [28]. It has been established that heterojunctioned AgPi-based structures such as AgPi/TiO_2 [29] and AgPi/Fe_2O_3 [30] nanocomposites improve charge separation of the photo-excited e^-/h^+ pairs, where they are mainly used in the photo-decomposition of organic contaminants.

In recent years, several researchers have claimed that the deposition of metal Ag over the surface of AgPi enhances the light harvesting efficiency, resulting in improved photocatalytic performance, as well as conferring higher stability under visible-light conditions [31–33]. Nevertheless, AgPi undergoes photocorrosion and leaching in aqueous solutions when irradiated with light, hampering its extensive use [34,35]. Ideally, the heterojunction photocatalyst comprising AgPi and monoclinic $BiVO_4$ should facilitate the separation of photo-excited e^-/h^+ pairs owing to its interlaced band structures. Very recently, we reported PEC water oxidation with Zr-doped $BiVO_4$ photocatalysts incorporated with AgPi nanoclusters (AgPi-Zr-$BiVO_4$) [36]. The fabricated AgPi-Zr-$BiVO_4$ photoanodes revealed a notable photocurrent density of 2.3 mA cm^{-2} at 1.23 V_{RHE}. Nevertheless, the AgPi/Zr:$BiVO_4$ photoanodes suffered a 25% photocurrent loss after 24 h of operation; however, these drawbacks can be easily resolved by modifying the surface with hole-conducting protection layers. In recent years, NiO_x and Ni-OH-Pi have been widely recognized as exceptional hole-conducting protection layers for electrodes because of their exceptional hole-transfer and electron-blocking nature owing to the comparatively higher CB edge positions [37–40].

In this study, controlled electrodeposition of a thin and homogenous nickel hydroxylphosphate Ni-OH-Pi nanoparticle film on the surface of a Zr:$BiVO_4$ photoanode is achieved, and the effects of the Ni-OH-Pi co-catalyst on increasing the PEC water oxidation and stability of the AgPi/Zr:$BiVO_4$ composite photoelectrodes (denoted AgNi-OH-Pi /Zr:$BiVO_4$) is established. A notable photocurrent density of ~3.0 mA cm^{-2} at 1.23 V vs. RHE was obtained after 60 h of continuous operation, and the observed activities is ascribed to the synergetic strong visible-light absorption and enhanced charge separation, as well as the exceptional transport and surface properties.

2. Materials and methods

2.1. Materials

Bismuth(III) nitrate [$Bi(NO_3)_3{\cdot}5H_2O$, ≥98.0%], vanadyl acetylacetonate [$VO(acac)_2$, ≥97.0%], zirconyl chloride octa-hydrate ($ZrCl_2O{\cdot}8H_2O$), nickel chloride hexahydrate ($NiCl_2{\cdot}6H_2O$, ≥98.0%), and sodium hydroxide (NaOH, ≥90%) were obtained from Sigma Aldrich. Dimethylsulfoxide (DMSO, ≥99.9%) and ethylene glycol (≥99%) were acquired from Sigma Aldrich. Sodium phosphate (monobasic and dibasic; NaH_2PO_4, ≥99.0% and Na_2HPO_4, ≥98.0%, Sigma Aldrich) were used to prepare the buffer solution. Hydrogen peroxide (H_2O_2) from J.T Baker was employed as a hole scavenger. A Millipore purification system (Synergy) was engaged to obtain high-purity water for preparation of the solutions. FTO-coated glass was obtained from Hartford glass (15 Ω cm^{-2}).

2.2. Synthesis of $BiVO_4$ and Zr-$BiVO_4$ electrodes

$BiVO_4$ photoanodes were fabricated via a two-step process reported by Choi and coworkers [41]. The (Zr) $BiVO_4$ photoanodes were fabricated according to a previously reported optimization process [42].

2.3. Sequential electrodeposition of Ag and Ni metal on Zr-$BiVO_4$ electrode

For the present study, bimetallic Ag/Ni nanostructured photoanodes were obtained by first mixing 0.02 M silver acetate and 0.02 M nickel chloride in DMSO solution. The fabricated solution was purged under a stream of argon for 15 min. Firstly, Ag was electrodeposited from the 0.02 M silver acetate solution by maintaining the potential at −2.0 V vs. Ag/AgCl, and the cathodic deposition was continued by altering the total deposition charge (5–30 mC cm^{-2}). Once the electrodeposition of Ag was optimized, deaerated 0.02 M $NiCl_2$ was added to the electrochemical cell, the solution was stirred, and electrodeposition was repeated (−2 V vs. Ag/AgCl) by changing the total deposition charge (10–50 mC cm^{-2}). Once the electrodeposition of Ag was complete, the photoanodes were removed and cleaned with Millipore water and left to air dry for 15 min prior to analysis. This sequential electrodeposition was performed to obtain the desired photoanodes.

2.4. Preparation of Ni Ag-OH-Pi on Zr:$BiVO_4$ photoanodes

After electrodeposition of the highly dispersed Ag and Ni metallic nanoparticles over the Zr-$BiVO_4$ photoanodes, the AgPi and Ni-OH-Pi films were incorporated using cyclic voltammetry (CV) in the range from −0.5 to 1.6 V (vs. Ag/AgCl) in 0.1 M PBS at pH 7.5. For comparison, Ag nanoparticle- and AgPi-decorated Zr-$BiVO_4$ photoanodes were fabricated by following the previously reported procedures.

2.5. Materials characterization

For the purpose of morphological characterization, the fabricated photoanodes were observed via field-emission scanning electron microscopy (FESEM, JSM 7000F JEOL) and transmission electron microscopy (TEM; JEM-2100 JEOL) at 200 kV. Diffuse reflectance and transmittance spectra were acquired via a Perkin Elmer 950 UV–vis spectrometer armed with an integrating sphere. A Rigaku XtaLAB Mini II benchtop X-Ray crystallography system (Cu-Kα radiation $\lambda = 0.154$ nm, scan speed: 3° min^{-1}) was employed for the X-ray diffraction measurements (XRD). Surface

analysis of the photoanodes was executed by means of X-ray photoelectron spectroscopy (XPS) using a Specs SAGE 150 instrument.

Control of the potential through CV, linear sweep voltammetry (LSV), and chronoamperometric analysis was achieved by means of an AutoLab potentiostat (PGSTAT30). PEC investigation of the photoanodes was performed using CV and LSV in the dark and under stimulated solar illumination (AM 1.5 G 100 mW cm^{-2}) in 0.1 M PBS (pH 7.5). Additionally, 0.5 M H_2O_2 (30%) was introduced as a hole scavenger to evaluate the efficiency of the charge transfer and charge separation. The fabricated photoanodes were investigated in a classical electrochemical cell in 3-electrode assembly [reference electrode = Ag/AgCl (3 M KCl), counter electrode = Pt wire]. A 300 W Xe lamp with a 1.5 AM solar filter was employed to stimulate sunlight. A photocurrent spectroscopy system (Instytut Fotonowy) armed with a 150 W X lamp coupled with a monochromator was employed for evaluation of the photocurrent generation efficiency (incident monochromatic photon to current conversion efficiency, IPCE). The IPCE for each wavelength was evaluated by applying Eq. (1):

$$IPCE\ \% = \frac{I_{ph}(A)}{P(W)} \times \frac{1239.8}{\lambda(\mathrm{nm})} \times 100 \quad (1)$$

where i_{ph} is the photocurrent density, P is the light power density, and λ is the wavelength of the light.

The absorbed photon to current efficiency (APCE) spectra were acquired from the equivalent IPCE and light harvesting efficiency (LHE) spectra. The *LHE* can be evaluated via Eq. (2):

$$LHE = 1 - 10^{-A_\lambda}, \quad (2)$$

where A_λ is the absorbance and λ is the wavelength. Thus, the APCE can be calculated according to Eq. (3):

$$APCE\ \% = \frac{IPCE}{LHE} \times 100, \quad (3)$$

The applied bias photon to current efficiency (ABPE) is given by:

$$ABPE\ (\%) = \frac{J_{PEC}(\mathrm{mA/cm^2}) * (1.23 - V_{bias})V}{Pin(\mathrm{mW/cm^2})} \times 100, \quad (4)$$

where J_{PEC} is the photocurrent density, V_{bias} is the applied bias, and P_{in} is the incident illumination power density (AM 1.5G). PEC oxygen generation was monitored with an oxygen analyzer (Oxysense Inc., TX, 300/5000 series).

The Faradaic efficiency of the photoanodes was calculated as follows:

$$FE\ (\%) = \frac{n(O2)evolved\ (\mathrm{mol})}{n(O2)theoretical\ (\mathrm{mol})} \times 100 \quad (5)$$

3. Results and discussion

Silver-nickel hydroxyphosphate (AgNi-OH-Pi) was decorated over Zr:$BiVO_4$ via a two-step electrodeposition process in an electrolyte comprising 0.02 M silver acetate and 0.02 M $NiCl_2$, followed by CV scans in 0.1 M PBS solution. Scheme S1 demonstrates the various stages of the synthesis procedure for obtaining the Ni-OH-Pi/Zr:$BiVO_4$ photoanodes. Notably, during the CV scans, the adsorbed water on the electrode surface tends to generate OH^- ions. Consequently, the OH ions react with Ni^{2+} to precipitate Ni hydroxide (Ni-OH) on the electrode surface, ensuing in the generation of AgNi-OH-Pi over the Zr:$BiVO_4$ photoanodes.

The morphology and microstructure during the various stages of fabrication of the photoanodes were examined by FE-SEM. The optimized nanostructured Zr:$BiVO_4$ films were decorated with Ag and Ni catalysts by a sequential two-step electrodeposition process, followed by electrochemical anodic oxidation in 0.1 M PBS at pH 7.5. For comparison, Fig. 1a display the FE-SEM micrographs of Zr:$BiVO_4$ photoanodes, with the optimum Zr addition (2.5 mol %), demonstrating that after the Zr incorporation over $BiVO_4$ surface, the electrodes keeps the smoother-edged dendrites with higher surface area. Fig. 1b displays the FE-SEM images of the Ni nanoparticles electrodeposited (charge: 40 mC cm^{-2}) on the Zr:$BiVO_4$ (Ni-Zr:$BiVO_4$) photoanodes. The FESEM images of Ni-Zr:$BiVO_4$ show that the Ni nanoparticle loading was uniform and thin enough so that there were no noticeable alterations to the structural morphology of the Zr-$BiVO_4$ photoanodes. The obtained Ni/Zr:$BiVO_4$ photoanodes were then converted to Ni-OH-Pi/Zr:$BiVO_4$ by electrochemical treatment (trough 15 CV scans) in 0.1 M PBS at pH 7.5 (Fig. 1b), as evidenced by energy dispersive spectroscopic (EDS) mapping analysis (Supporting Information, Fig. S1). The FESEM images of Ni-OH-Pi/Zr:$BiVO_4$ evidently display that the surface of $BiVO_4$ became homogenously smoother after the incorporation of phosphate (Fig. 1c). Fig. 1d displays the FE-SEM images of the Ag and Ni nanoparticles electrodeposited (charge: 40 mC cm^{-2}) (0.25:1 v/v) on the Zr:$BiVO_4$ photoanodes with an average diameter of 5–10 nm. After deposition of the AgNi nanoparticles on the photoanodes, the electrode surface became uniformly rougher due to Ni/Zr-$BiVO_4$. Finally, as shown in Fig. 1e, the morphology of the AgNi nanoparticles changed after the electrochemical anodic oxidation treatment (through 15 CV scans) in 0.1 M PBS at pH 7.5, related to the formation of AgPi [41] and Ni-OH-Pi nanoparticles on the surface of the Zr:$BiVO_4$ photoanodes (Fig. 1e). The modification of the element distribution in the Zr:$BiVO_4$ photoanodes was further examined by EDS mapping. The variations of the Bi-Lα, V-Lα, Zr-Kα, Ag-Lα, Ni-Kα, and P-Lα signals along the Zr:$BiVO_4$ photoanode are given in the Supporting Information, Fig. S2. Evidently, the distribution of Ag and Ni along the Zr:$BiVO_4$ photoanodes was uniform.

For HR-TEM analysis, the photoanodes were fabricated by scratching off the films on a Cu grid. The as-prepared bimetallic AgNi nanoparticles deposited on the surface of the Zr:$BiVO_4$ electrode via cathodic electrodeposition were further evidenced by TEM (Fig. 2a). Interplanar spacings of 0.31 and 0.28 nm were apparent from Fig. 2b, consistent with the (−1 1 1) and (1 1 1) crystallographic planes of monoclinic ZrO_2 (CAS number 1309-37-1), correspondingly. The fringe spacings of 0.235 and 0.205 nm relate to the (1 1 1) plane of the metallic Ag and Ni nanoparticles of Zr:$BiVO_4$, correspondingly. The results evidence that the deposition of Ag and Ni on the Zr:$BiVO_4$ surface, which led to a good association between Ag, Ni, and Zr-doped $BiVO_4$, was successfully achieved. In particular, the HR-TEM observations revealed the absence of lattice fringes related to AgPi or Ni-OH-Pi nanoparticles (Fig. 2c and d, respectively), undoubtedly owing to the low-crystallinity after electrochemical treatment.

UV–vis diffuse reflectance spectroscopy was used to assess the optical bandgap and absorption of the fabricated photoanodes, as shown in Fig. 3a. The deposition of Ag and Ni phosphate nanoparticles also led to enhanced optical density of the Zr:$BiVO_4$ photoanodes in the visible-light range due to the electron transition at the band edges of the monoclinic-scheelite phase Zr:$BiVO_4$. The AgNi-OH-Pi/Zr:$BiVO_4$ photoanodes exhibited the optimal light absorption, indicating that the combined deposition of AgPi and Ni-OH-Pi provides synergistic enhancement of the optical density. Fig. 3a (inset) shows the relationship between $(\alpha h\nu)^{1/2}$ and E (eV) for Zr:$BiVO_4$ and AgNi-OH-Pi/Zr:$BiVO_4$, with bandgaps of 2.41 and 2.32 eV, respectively. This illustrates that the thin layer coating on the AgNi-OH-Pi particles can contribute to the absorption of more visible-light photons [36]; nevertheless, whether the enhanced photon absorption truly results in an improved photocurrent response cannot be substantiated by the absorption data alone and requires wavelength-dependent photocurrent analysis, as presented below. It should also be noted that, earlier works have

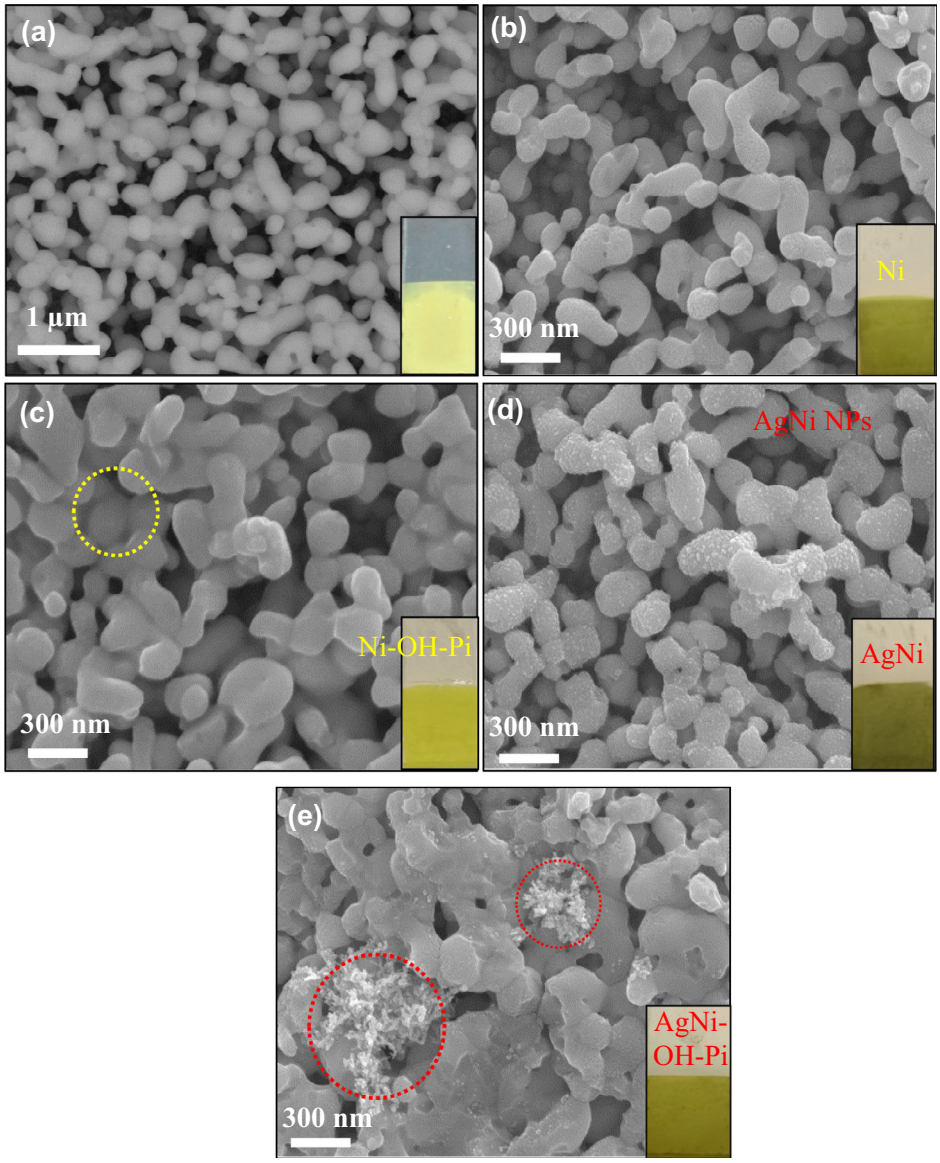

Fig. 1. FE-SEM micrographs of the (a) Zr:$BiVO_4$ photoanodes fabricated using electrodeposition process; (b) Ni/Zr:$BiVO_4$ photoanodes displaying the as-synthesized Ni nanoparticles, (c) Ni-OH-Pi/Zr:$BiVO_4$ photoanodes obtained after 20 cycles in PBS and smoothed interface is shown by a dotted yellow colored circle, (d) AgNi/Zr:$BiVO_4$ film showing the uniform and densely anchored Ag and Ni nanoparticles and (d) AgNi-OH-Pi/Zr:$BiVO_4$ photoanodes obtained after 20 cycles in PBS and yellow colored dotted circles showing the agglomerated Ni-Ag phosphate particles over the $BiVO_4$ surface.

evidenced that the Ag/AgPi nanoparticles induce light scattering [34], as illustrated by the increased optical absorbance at wavelength >550 nm in Fig. 3a.

Structural analysis of the developed composites was performed by XRD (Fig. 3b). For the as-made $BiVO_4$, sharp peaks attributed to the $BiVO_4$ phase, matching the standard CAS file number 00-014-0688, were observed. The patterns also demonstrate the low intensity of the XRD peaks owing to the low relative content of Ag and Ni. There were no significant changes in the diffraction patterns of AgNi-OH-Pi, illustrating that there is no establishment of new phases in fabricated photoanodes. Compared with the HR-TEM results, this provides evidence that the as-made AgNi-OH-Pi photoanodes have both short-range order and long-range disordered structures.

Further confirmation of conversion of the bimetallic nanoparticles of Ag and Ni into AgNi-OH-Pi through the electrochemical treatment was evidenced by XPS. The full XPS spectrum (Fig. S4) indicates that the AgNi-OH-Pi/Zr:$BiVO_4$ composite comprised Bi, V, Zr, Ag, Ni, P, and O, compared with the AgNi/Zr:$BiVO_4$ composite before electrochemical treatment in 0.1 PBS (pH 7.5). The asymmetry of the Ag 3d equivalent signal evidences the existence of various oxidation states of Ag on the AgPi/Zr:$BiVO_4$ photoanodes. After deconvolution of the Ag 3d signal (Fig. 4a), two major signals at 374.3 and 368.3 eV were resolved, agreeing with the Ag $3d_{3/2}$ and Ag $3d_{5/2}$ orbitals of Ag^+, receptively. These results agree with earlier works [43,44], suggesting the oxidation of metallic Ag during the electrochemical treatment. Furthermore, distinctive Ag^0 signals were also apparent at 376.8 and 368.7 eV, with lower intensity, suggesting the presence of metallic Ag, which is highly beneficial for improving the charge separation and inhibiting the reductive decomposition of AgPi [45,46]. The high-resolution spectrum of Ni $2p_{3/2}$ showed two peaks (Fig. 4b). The peak at 858.8 eV is attributed to Ni cations in an octahedral environment, consistent with nickel hydroxylphosphate [39,40]. The other peak at 852.8 eV is distinctive of the Ni-OH species. The high-resolution spectrum of the asymmetrical O 1s signal at 531.8 eV in the XPS profile of AgPi

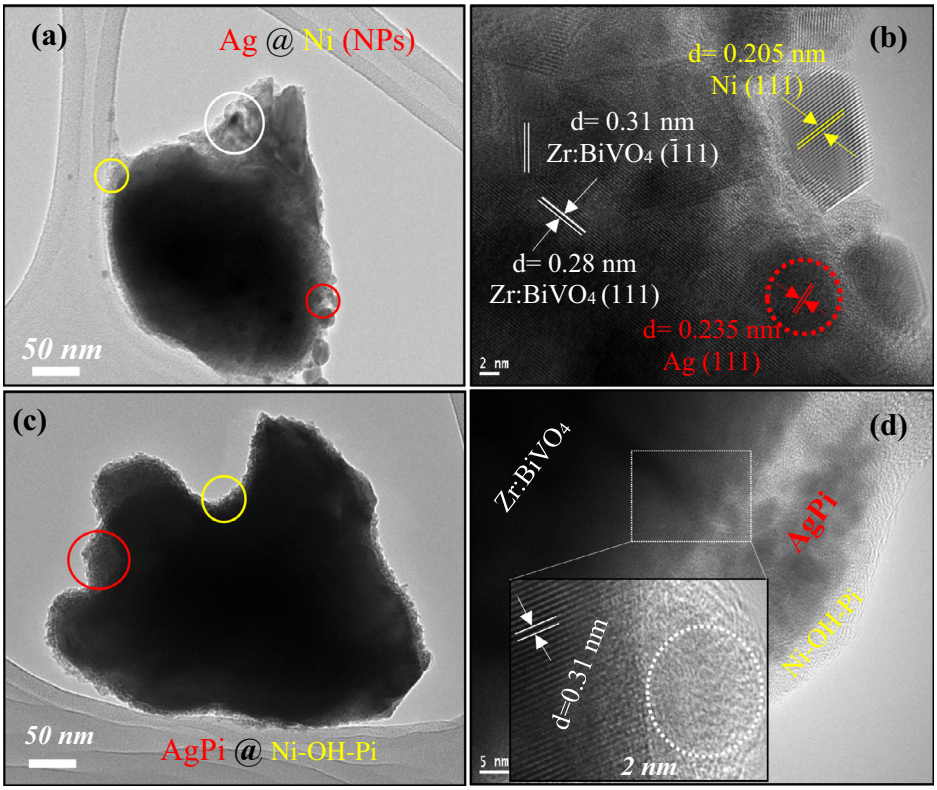

Fig. 2. HR-TEM images of (a) and (b) AgNi/Zr:$BiVO_4$ nanoparticles, displaying the (1 1 1) planes attributed to the Ag particles recorded from red dotted circle and (1 1 1) planes corresponding to the Ni particle recorded with red dotted circle. (c) and (d) AgNi-OH-Pi amorphous nanoparticles after phosphate modification on Zr:$BiVO_4$ photoelectrode recorded with white colored dotted circle.

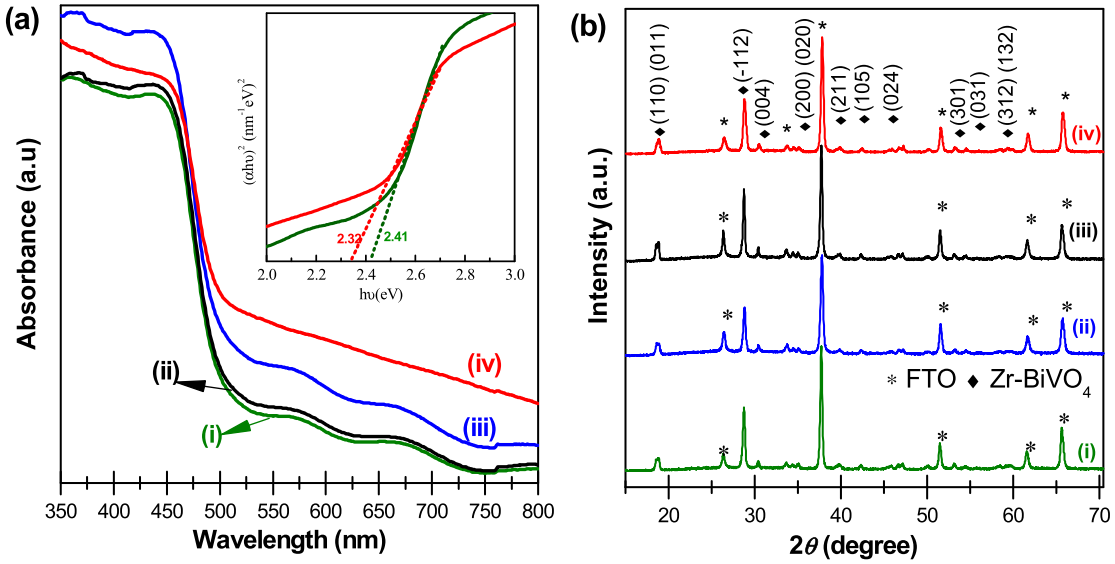

Fig. 3. (a) UV–vis absorption spectra and (b) XRD patterns of the as-prepared photoanodes (i) Zr:$BiVO_4$, (ii) Ni-OH-Pi/Zr:$BiVO_4$, (iii) AgPi/Zr:BiVO4, and (iv) AgNi-OH-Pi/Zr:$BiVO_4$. The inset of (a) shows the relationship between $(\alpha h\upsilon)^{1/2}$ and E (eV) for Zr:$BiVO_4$ and AgNi-OH-Pi/Zr:$BiVO_4$, with bandgaps of 2.41 and 2.32 eV, respectively.

and Ni-OH-Pi is shown in Fig. 4c. This peak was assigned to the phosphate groups as the peak could be separated into three different peaks at 530.3, 532.8, and 531.8 eV [47]. Moreover, the HRXPS spectrum in Fig. 4d shows a P 2p signal at 531.8 eV, attributed to the Ag-O, Ni-O, or P-O bonds on the surface; the peak at 532.6 eV is associated with the P–O and P–O–Ag or P–O–Ni combinations, and the other at 532.6 eV is associated with the P–OH group [48–50]. This indicates that the AgPi and Ni-OH-Pi nanoparticles were successfully prepared during the electrochemical treatment in 0.1 PBS (pH 7.5).

A three-electrode arrangement was used for PEC analysis in 0.1 M PBS (pH 7.5) under AM 1.5G simulated sunlight. The conditions for electrodeposition of the Ni nanoparticles were first optimized by varying the total charge used for Ni deposition (0–50 mC cm^{-2}) (Fig. S5a). The optimized charge density for deposition at the highest photocurrent density was 40 mC cm^{-2}. Indeed,

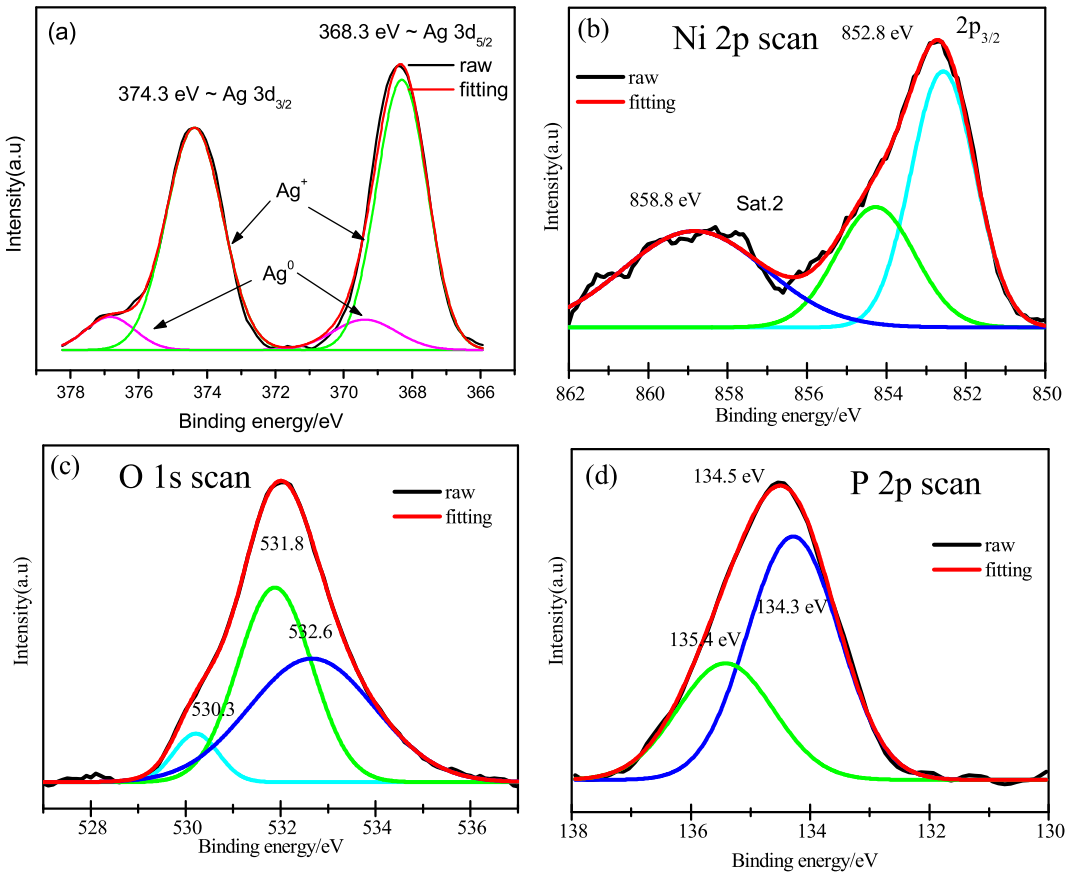

Fig. 4. HR-XPS spectra of (a) Ag 3d, (b) Ni 2p, (c) O 1s, (d) and P 2p characteristic regions for the AgNi-OH-Pi/Zr-$BiVO_4$ electrode.

our previous studies have demonstrated that a maximum electrodeposition charge of 10 mC cm^{-2} is adequate for deposition of the Ag nanoparticles. To optimize the mixing ratio, Ag/Ni was added to the electrodeposition bath in the same molar concentration (0.01 M). The best performance was obtained with a mixing ratio of 0.25:1 *v/v* at a constant charge density of 30 mC cm^{-2} (Supporting Information, Fig. S5a). The electrodeposition conditions for achieving the best Ag/Ni volume mixing of the nanoparticles was then optimized by varying the total charge (5–40 mC cm^{-2}) (Supporting Information, Fig. S5b).

The optimal deposition charge density for maximizing the photocurrent density was 30 mC cm^{-2}. The characteristic photocurrent–potential (*J–V*) plots for the PEC water oxidation in Fig. 5a (and Supporting Information, Fig. S6) confirm that the optimized AgNi-OH-Pi/Zr:$BiVO_4$ sample exhibited enhanced photocurrents compared with AgPi/Zr:$BiVO_4$, Ni-OH-Pi/Zr:$BiVO_4$, Zr:$BiVO_4$, and bare $BiVO_4$. The photocurrent density increased significantly with the bias voltage and reached ~3.2 mA cm^{-2} at 1.23 V vs. RHE in 0.1 PBS (pH 7.5), which corresponds to an 8-fold enhancement compared with that obtained with the Zr:$BiVO_4$ photoanodes. The photocurrent onset potentials (V_{on}) for all of the photoanodes were resolved from the quasi-steady-state *J–V* curves obtained at photocurrents of 1 m Vs^{-1} and 0.1 mA cm^{-2}, and the obtained values were 0.25 V vs. RHE for AgNi-OH- Pi/Zr:$BiVO_4$ and 0.85 V vs. RHE for Zr:$BiVO_4$ (Fig. 5b). A higher photocurrent density was also obtained in the low bias region (0.6 V) compared with the other samples, as shown in Fig. 5c. Hence, the *J–V* data were acquired in the absence and presence of H_2O_2 to investigate the limitation of the PEC performance of the Zr-$BiVO_4$ and AgNi-OH-Pi/Zr:$BiVO_4$ photoanodes (Fig. 5d). In the attendance of H_2O_2, the *J–V* curves of Zr-$BiVO_4$ showed a significant, but anticipated, enhancement in both the onset potential (0.24 V) and the photocurrent density at 1.23 V vs. RHE (~3.2 mA cm^{-2}). Interestingly, these results agree with the PEC performance of the optimized AgNi-OH-Pi/Zr:$BiVO_4$ photoanodes (Fig. 5c, Supporting Information, Fig. S5 and Table S1). Based on these comparisons, it is evident that a combination Ag and Ni phosphate nanoparticles is required to satisfy the demand for higher efficiency and stability.

Fig. 6a shows the long-standing stability of AgNi-OH-Pi/Zr:$BiVO_4$ at 1.23 V vs. RHE based on the *J–t* data acquired in 0.1 M PBS (pH 7.5) over 60 h, with a photocurrent density of ~3.0 mA cm^{-2}; there was no obvious decay, signifying the exceptional long standing stability. In comparison, the AgPi/Zr:$BiVO_4$ electrode, for which the chemical dissolution of Zr:$BiVO_4$ was suppressed, displayed a significant improvement in the photocurrent stability within 10 h; however, after the 10th hour, the photocurrent stability gradually declined as a result of the photocorrosion of Zr:$BiVO_4$, although it was still detected. Conversely, rapid photocurrent decay was observed for the Zr:$BiVO_4$ electrode within 1100 s, partly due to its chemical and PEC instability. This instability is due to the anodic photocorrosion of Zr:$BiVO_4$ produced from the accumulation of holes at the interface as a result of the slow transfer kinetics of the Zr:$BiVO_4$ interfacial hole generated by water oxidation. Once Ni (as Ni-OH-Pi) was added, the photocurrent of the resulting AgNi-OH-Pi/Zr:$BiVO_4$ electrode became more stable, and a photocurrent density of 2.99 mA cm^{-2} was retained after 60 h. The XRD patterns and FE-SEM images of AgNi-OH-Pi/Zr:$BiVO_4$ were acquired at 60 h to examine the mass loss of Zr:$BiVO_4$ during the *J–t* measurement. The XRD pattern and FESEM image of AgNi-OH-Pi/Zr:$BiVO_4$ acquired at 60 h showed no detectable changes compared with that of AgPi/Zr:$BiVO_4$ acquired before 30 h (Figs. 6b and c, S3). However, the XRD pattern of AgPi/Zr:

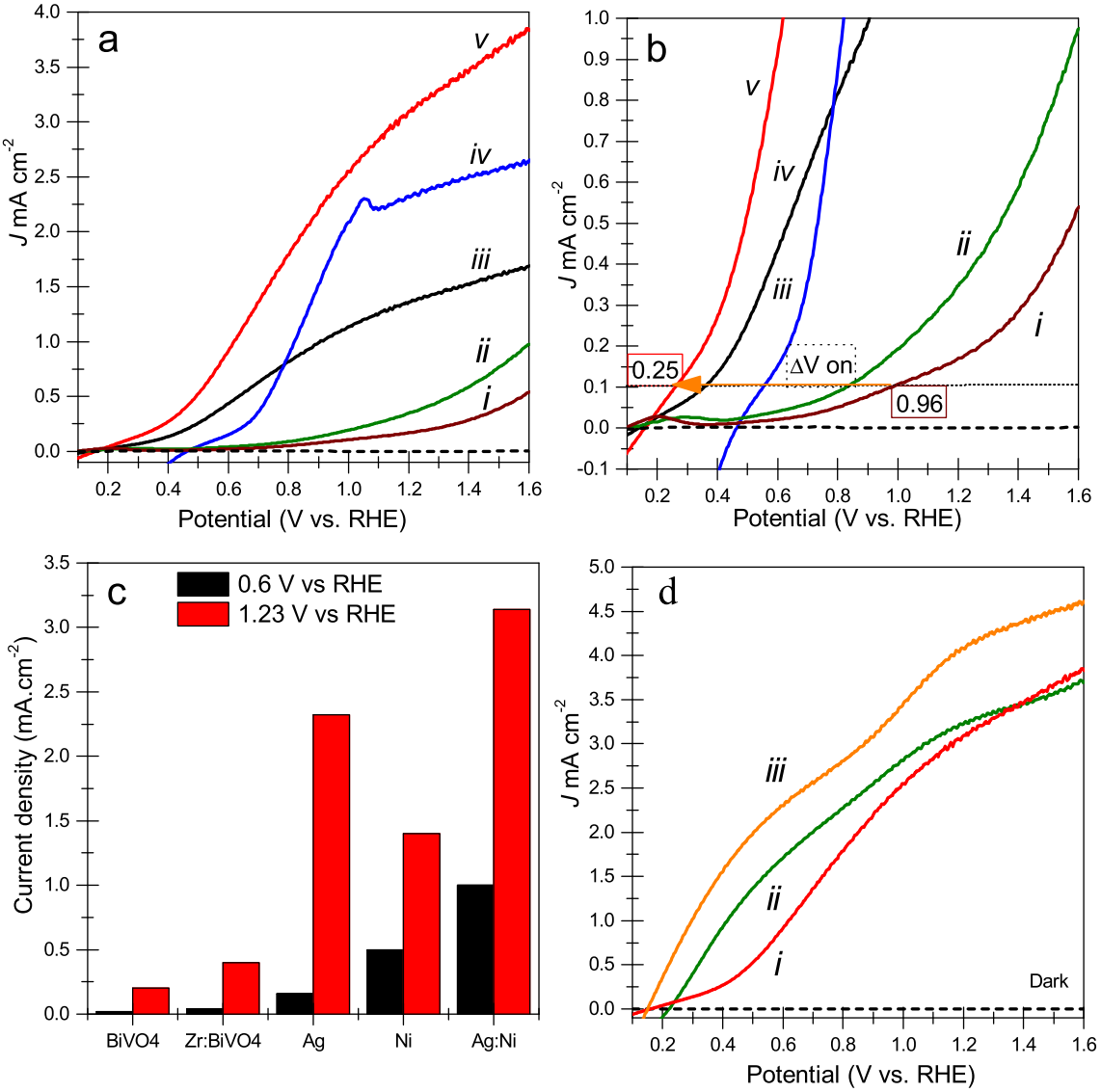

Fig. 5. (a) LSV characteristics of (i) bare $BiVO_4$, (ii) Zr:$BiVO_4$ (Zr molar concentration 2.5%), (iii) Ni-OH-Pi/Zr:$BiVO_4$ (40 mC-Ni), (iv) AgPi/Zr:$BiVO_4$ (10 mC-Ag), and (v) AgNi-OH-Pi/Zr:$BiVO_4$ (30 mC-Ag/Ni 0.25/1 *v*//*v*) photoanodes measured in 0.1 M PBS (pH 7.5) under illumination (AM 1.5G, 100 mW cm^{-2}, scan rate = 50 mV s^{-1}). (b) LSVs displaying photocurrent onset potentials for all electrodes. (c) Changes in the photocurrent for all photoelectrodes in 0.1 M PBS (pH 7.5) at 0.6 and 1.23 V versus RHE under illumination. (d) Comparison of LSVs of the (i) AgNi-OH-Pi/Zr:$BiVO_4$ photoanodes using 0.1 M PBS (pH 7.5) with (ii) Zr:$BiVO_4$ and (iii) AgNi-OH-Pi/Zr:$BiVO_4$ photoanodes using 0.1 M PBS (pH 7.5) with 0.5 M H_2O_2 as a hole scavenger.

$BiVO_4$ acquired at 30 h demonstrated a decrease in the intensity of the peaks of Zr:$BiVO_4$ (Fig. 6c).

Because the Zr:$BiVO_4$ nanoparticles were modified with various amounts of metal phosphate, resulting in different colors, further examination of their wavelength-dependent PEC behavior was required to recognize the interplay between the photocatalytic performance and light absorption of these electrodes. Fig. 7a and b show the IPCE and ACPE data. The IPCE values were calculated via eqn: $IPCE\% = \frac{I_{ph}(A)}{P(W)} \times \frac{1239.8}{\lambda\ (nm)} \times 100$, where I_{ph} is the measured photocurrent density at a specific wavelength, P is the light power density, and λ is the wavelength of the light. The APCE can be calculated according to Eq. (3), and $APCE\% = \frac{IPCE}{LHE} \times 100$, where $LHE = 1 - 10^{-A_\lambda}$.

The IPCE of AgNi-OH-Pi/Zr:$BiVO_4$ was compared with that of AgPi/Zr:$BiVO_4$ and Ni-OH-Pi/Zr:$BiVO_4$ at 1.23 V using a monochromator (Fig. 7a). The onset of the IPCE was at 545 and 523 nm for the AgNi-OH-Pi/Zr:$BiVO_4$ and AgPi/Zr:$BiVO_4$ photoelectrodes, respectively. These findings show that the AgNi-OH-Pi layer acts as an extra photon absorber, utilizing more visible light for photocurrent production, even though there was no additional absorption by the existing AgPi phase, as observed from the UV–vis spectrum of the AgPi/Zr:$BiVO_4$ photoelectrode. The IPCE and APCE values were higher for the AgNi-OH-Pi/Zr:$BiVO_4$ photoelectrode compared with those of the Ni-OH-Pi/Zr:$BiVO_4$ photoelectrode (Fig. 7a and b). This illustrates the advantages of the AgPi layer that facilitates electron–hole separation in the Zr:$BiVO_4$ layer by allowing quick hole extraction from the VB of Zr:$BiVO_4$ to the VB of AgPi [31]. The rate of O_2 evolution with the AgNi-OH-Pi/Zr:$BiVO_4$ photoelectrode was compared with that of AgPi/Zr:$BiVO_4$ and Ni-OH-Pi/Zr:$BiVO_4$, as shown in Fig. 7c. The AgNi-OH-Pi/Zr:$BiVO_4$ photoelectrode displayed the maximum activity for O_2 evolution (81.0 μmol cm^{-2}) compared to AgPi/Zr:$BiVO_4$ (50 μmol cm^{-2}) and Ni-OH-Pi/Zr:$BiVO_4$ (28.5 μmol cm^{-2}), indicating that AgNi-OH-Pi is more effective for separating the photogenerated charges in Zr:$BiVO_4$ than AgPi and Ni-OH-Pi. Moreover, Fig. S8 (Supporting Information) displays the theoretical and experimental oxygen evolution for the AgNi-OH-Pi/Zr:$BiVO_4$ photoelectrode during the

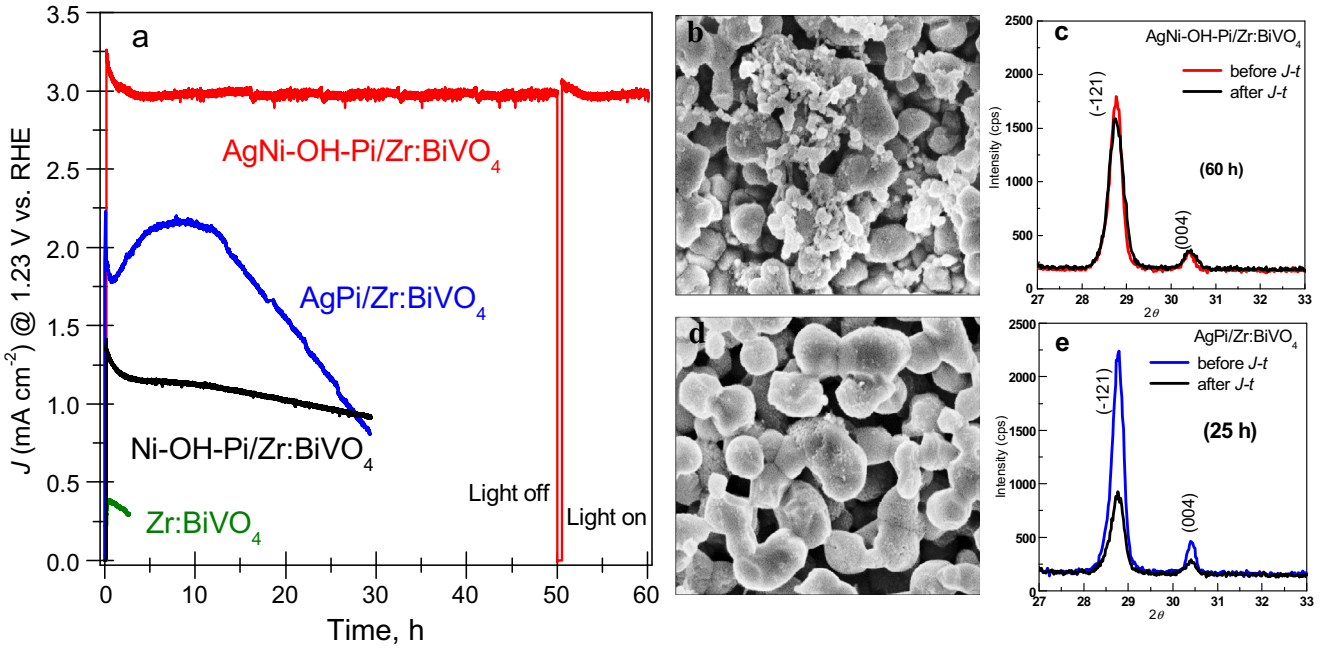

Fig. 6. (a) *J–t* curves for analysis of the long-term photostability of the AgNi-OH-Pi/Zr:$BiVO_4$ (red), AgPi/Zr:$BiVO_4$ (blue), and Ni-OH-Pi/Zr:$BiVO_4$ (black) photoanodes compared with Zr:$BiVO_4$ (olive), measured in 0.1 M PBS (pH 7.5) at 1.23 V vs. RHE for 60, 30, 30, and 2.5 h, respectively, under illumination (AM 1.5 G) for all samples. (b) SEM image of the AgNi-OH-Pi/Zr:$BiVO_4$ photoanode taken after *J–t* measurement for 60 h in 0.1 M PBS (pH 7.5). (c) XRD patterns of AgNi-OH-Pi/Zr:$BiVO_4$ photoanode before (black) and after (red) 60 h of *J–t* measurement in 0.1 M PBS (pH 7.5). (d) SEM image of AgPi/Zr:$BiVO_4$ photoanode taken after 25 h of *J–t* measurement in 0.1 M PBS (pH 7.5). (e) XRD patterns of AgPi/Zr:$BiVO_4$ photoanode before (black) and after (blue) 25 h of *J–t* measurement in 0.1 M PBS (pH 7.5).

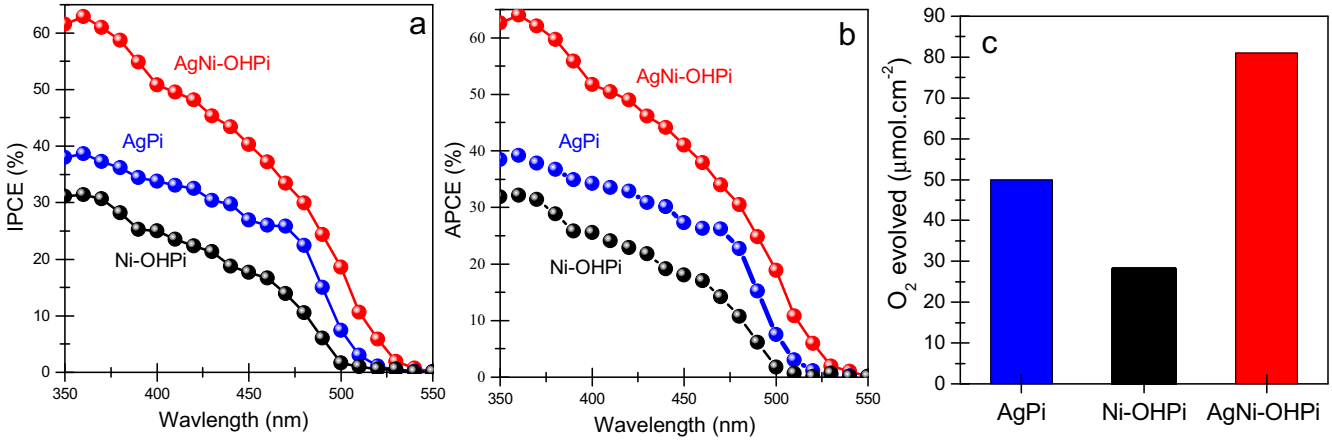

Fig. 7. (a) IPCE and (b) APCE spectra of the Ni-OH-Pi-, AgPi-, AgNi-OH-Pi-incorporated Zr:$BiVO_4$ photoanodes measured at 1.23 V vs. RHE in 0.1 M PBS (pH 7.5) with the standard three-electrode system and (c) comparison of the maximum O_2 evolution for the Zr:$BiVO_4$-based photoelectrodes.

measurements; the faradaic efficiency was almost 90% after 3 h, and eventually saturated at ~98%.

The band-edge potential of the fabricated photoanode was examined by PEC impedance spectroscopy (PEIS). The Nyquist plots of the AgNi-OH-Pi/Zr:$BiVO_4$ photoanodes evaluated under illumination at 1.0 V vs. RHE and the matching equivalent circuit are displayed in Fig. 8a. This clearly shows that the diameter of the arc radius on the PEIS Nyquist plot of the AgNi-OH-Pi/Zr:$BiVO_4$ photoanode was much smaller than that of the reference photoanodes. The smaller radius implies that the AgNi-OH-Pi/Zr:$BiVO_4$ photoanodes demonstrated rapid interfacial charge transfer and more effective separation of the photoinduced hole/electron pairs than the parent photoanodes. The obtained capacitance values were in the 10^{-5}–10^{-4} F cm^{-2} region, indicating a major contribution of the double layer capacitance at the intermediate voltages, mostly dominated by $BiVO_4$ (Fig. 8b). The capacitive peak at 0.8 V vs. RHE due to the V^{4+}/V^{5+} redox couple also provides clear evidence of the dominant $BiVO_4$ phase [34]. However, a charge transfer resistance (R_{CT}) of >1 kΩ at 1.0 V vs. RHE for the AgNi-OH-Pi/Zr:$BiVO_4$ photoanode, with a considerably higher bias (>0.8 V), is required for the Zr-$BiVO_4$ photoanodes (Fig. 8b). The constant capacitance and decrease in the R_{CT} at the same voltages strongly suggests that AgNi-OH-Pi performs as an active electrocatalytic material, improving the charge transfer kinetics and suppressing surface recombination.

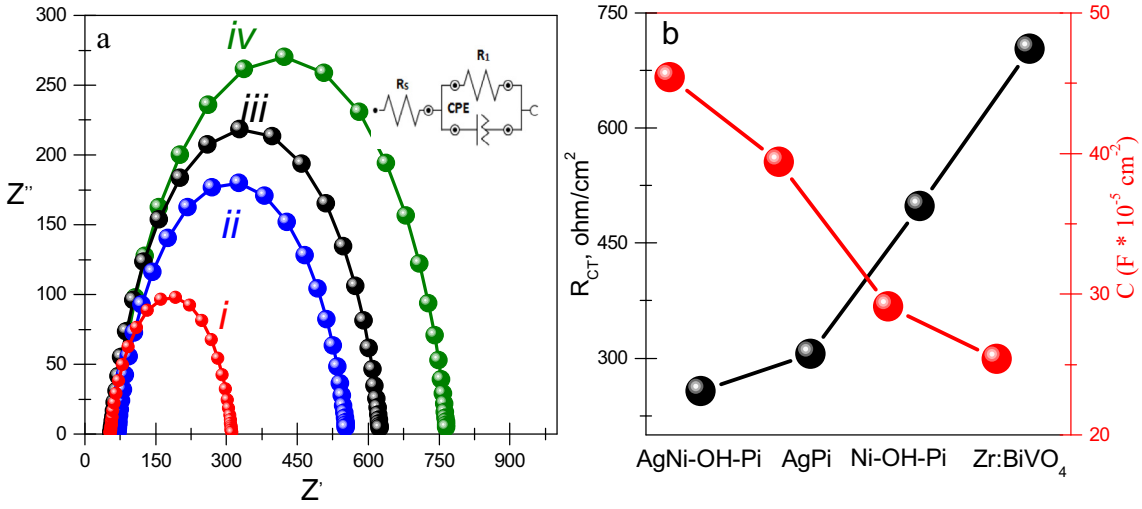

Fig. 8. (a) Photoelectrochemical impedance spectra of the (i) AgNi-OH-Pi/Zr:$BiVO_4$ photoanode compared with the (ii) AgPi/Zr:$BiVO_4$, (iii) Ni-OH-Pi/Zr:$BiVO_4$, and (iv) Zr:$BiVO_4$ photoanodes. The Nyquist plots were acquired at 1.0 V vs. RHE in the a.c. potential frequency range of 100,000–0.05 Hz. The inset shows the equivalent circuit and (b) charge transfer resistance and capacitance for all electrodes at 1.0 V vs. RHE, measured by fitting the PEIS data to a simple Randles circuit.

4. Conclusions

A conformal coating of Ni-OH-Pi, AgPi, and AgNi-OH-Pi layers on a Zr:$BiVO_4$ electrode was achieved via electrochemical deposition and electrochemical treatment methods. The uniform Ni-OH-Pi layer showed excellent protection from chemical dissolution in a pH 7.5 solution. When the surface of Zr:$BiVO_4$ was modified with AgPi and Ni-OH-Pi, the resulting AgNi-OH-Pi/Zr:$BiVO_4$ photoanodes showed a photocurrent density of ~3.14 mA cm^{-2} at 1.23 V vs. RHE. The IPCE and APCE data, together with the absorption spectra, show that the Ag-Ni-OH-Pi layer serves as a protective layer and promotes photocurrent generation by increasing the photon absorption and hole/electron separation of the Zr:$BiVO_4$ layer. The excellent photoelectrocatalytic activity and stability as well as the fast, facile, and controllable industrial-scale fabrication of the AgNi-OH-Pi photoanodes suggest that it is a promising alternative to metal-oxide-protected water splitting photoanodes.

Acknowledgements

The authors are grateful to the Deanship of Scientific Research, King Saud University for funding through Vice Deanship of Scientific Research Chairs. The authors also thank the Deanship of Scientific Research and RSSU at King Saud University for their technical support.

Appendix A. Supplementary material

Electronic Supplementary Information is Available: Schematic representation of fabrication of the AgNi-OH-Pi/Zr:$BiVO_4$ photoanodes, SEM, EDS, and EDX mapping analysis, $J-V$ curves of the different samples under continuous illumination, optimization of the method of deposition of the AgPi, Ni-OH-Pi and AgNi-OH-Pi nanostructures, tables with optimized photocurrents with and without H_2O_2, XPS spectra, and $J-t$ measurements. Supplementary data to this article can be found online at https://doi.org/10.1016/j.jcat.2019.01.024.

References

[1] J.H. Montoya, L.C. Seitz, P. Chakthranont, A. Vojvodic, T.F. Jaramillo, J.K. Nørskov, Materials for solar fuels and chemicals, Nat. Mater. 16 (2017) 70.
[2] M.G. Walter, E.L. Warren, J.R. McKone, S.W. Boettcher, Q. Mi, E.A. Santori, N.S. Lewis, Solar water splitting cells, Chem. Rev. 110 (2010) 6446–6473.
[3] B.A. Pinaud, J.D. Benck, L.C. Seitz, A.J. Forman, Z. Chen, T.G. Deutsch, B.D. James, K.N. Baum, G.N. Baum, S. Ardo, Technical and economic feasibility of centralized facilities for solar hydrogen production via photocatalysis and photoelectrochemistry, Energy Environ. Sci. 6 (2013) 1983–2002.
[4] A. Fujishima, K. Honda, Electrochemical photolysis of water at a semiconductor electrode, Nature 238 (1972) 37.
[5] C. Du, X. Yang, M.T. Mayer, H. Hoyt, J. Xie, G. McMahon, G. Bischoping, D. Wang, Hematite-based water splitting with low turn-on voltages, Angew. Chem. Int. Ed. 52 (2013) 12692–12695.
[6] J.-W. Jang, C. Du, Y. Ye, Y. Lin, X. Yao, J. Thorne, E. Liu, G. McMahon, J. Zhu, A. Javey, Enabling unassisted solar water splitting by iron oxide and silicon, Nat. Commun. 6 (2015) 7447.
[7] J. Brillet, J.-H. Yum, M. Cornuz, T. Hisatomi, R. Solarska, J. Augustynski, M. Graetzel, K. Sivula, Highly efficient water splitting by a dual-absorber tandem cell, Nat. Photon. 6 (2012) 824.
[8] S.K. Deb, Opportunities and challenges in science and technology of WO_3 for electrochromic and related applications, Sol. Energy Mater. Sol. Cells 92 (2008) 245–258.
[9] F.F. Abdi, L. Han, A.H. Smets, M. Zeman, B. Dam, R. Van De Krol, Efficient solar water splitting by enhanced charge separation in a bismuth vanadate-silicon tandem photoelectrode, Nat. Commun. 4 (2013) 2195.
[10] T.W. Kim, K.-S. Choi, Nanoporous $BiVO_4$ photoanodes with dual-layer oxygen evolution catalysts for solar water splitting, Science (2014) 1245026.
[11] X. Shi, K. Zhang, K. Shin, M. Ma, J. Kwon, I.T. Choi, J.K. Kim, H.K. Kim, D.H. Wang, J.H. Park, Unassisted photoelectrochemical water splitting beyond 5.7% solar-to-hydrogen conversion efficiency by a wireless monolithic photoanode/dye-sensitised solar cell tandem device, Nano Energy 13 (2015) 182–191.
[12] M.N. Shaddad, P. Arunachalam, J. Labis, M. Hezam, A.M. Al-Mayouf, Fabrication of robust nanostructured (Zr) $BiVO_4$/nickel hexacyanoferrate core/shell photoanodes for solar water splitting, Appl. Catal. B 244 (2019) 863–870.
[13] A. Malathi, J. Madhavan, M. Ashokkumar, P. Arunachalam, A review on $BiVO_4$ photocatalyst: activity enhancement methods for solar photocatalytic applications, Appl. Catal. A 555 (2018) 47–74.
[14] A. Malathi, V. Vasanthakumar, P. Arunachalam, J. Madhavan, M.A. Ghanem, A low cost additive-free facile synthesis of $BiFeWO_6$/$BiVO_4$ nanocomposite with enhanced visible-light induced photocatalytic activity, J. Colloid Interface Sci. 506 (2017) 553–563.
[15] A. Kudo, K. Omori, H. Kato, A novel aqueous process for preparation of crystal form-controlled and highly crystalline $BiVO_4$ powder from layered vanadates at room temperature and its photocatalytic and photophysical properties, J. Am. Chem. Soc. 121 (1999) 11459–11467.
[16] Y. Park, K.J. McDonald, K.-S. Choi, Progress in bismuth vanadate photoanodes for use in solar water oxidation, Chem. Soc. Rev. 42 (2013) 2321–2337.
[17] K. Sivula, F. Le Formal, M. Grätzel, Solar water splitting: progress using hematite (α-Fe_2O_3) photoelectrodes, ChemSusChem 4 (2011) 432–449.
[18] Y. Ma, F. Le Formal, A. Kafizas, S.R. Pendlebury, J.R. Durrant, Efficient suppression of back electron/hole recombination in cobalt phosphate surface-modified undoped bismuth vanadate photoanodes, J. Mater. Chem. A 3 (2015) 20649–20657.
[19] L. Trotochaud, S.L. Young, J.K. Ranney, S.W. Boettcher, Nickel–iron oxyhydroxide oxygen-evolution electrocatalysts: the role of intentional and incidental iron incorporation, J. Am. Chem. Soc. 136 (2014) 6744–6753.
[20] D.K. Zhong, S. Choi, D.R. Gamelin, Near-complete suppression of surface recombination in solar photoelectrolysis by "Co-Pi" catalyst-modified W:$BiVO_4$, J. Am. Chem. Soc. 133 (2011) 18370–18377.

[21] P. Arunachalam, A. Al-Mayouf, M.A. Ghanem, M.N. Shaddad, M.T. Weller, Photoelectrochemical oxidation of water using La (Ta, Nb) O_2N modified electrodes, Int. J. Hydrogen Energy 41 (2016) 11644–11652.
[22] M.N. Shaddad, P. Arunachalam, A.M. Al-Mayouf, M.A. Ghanem, A.I. Alharthi, Enhanced photoelectrochemical oxidation of alkali water over cobalt phosphate (Co-Pi) catalyst-modified $ZnLaTaON_2$ photoanodes, Ionics (2018), https://doi.org/10.1007/s11581-018-2688-y.
[23] C. Zachäus, F.F. Abdi, L.M. Peter, R. Van De Krol, Photocurrent of $BiVO_4$ is limited by surface recombination, not surface catalysis, Chem. Sci. 8 (2017) 3712–3719.
[24] G.-F. Huang, Z.-L. Ma, W.-Q. Huang, Y. Tian, C. Jiao, Z.-M. Yang, Z. Wan, A. Pan, Ag_3PO_4 semiconductor photocatalyst: possibilities and challenges, J. Nanomater. 2013 (2013) 1.
[25] J. Pan, G. Liu, Facet control of photocatalysts for water splitting, Semicond. Semimetals 97 (2017) 349–391.
[26] X. Ma, B. Lu, D. Li, R. Shi, C. Pan, Y. Zhu, Origin of photocatalytic activation of silver orthophosphate from first-principles, J. Phys. Chem. C 115 (2011) 4680–4687.
[27] Z. Yi, J. Ye, N. Kikugawa, T. Kako, S. Ouyang, H. Stuart-Williams, H. Yang, J. Cao, W. Luo, Z. Li, An orthophosphate semiconductor with photooxidation properties under visible-light irradiation, Nat. Mater. 9 (2010) 559.
[28] A. Indra, P.W. Menezes, M. Schwarze, M. Driess, Visible light driven non-sacrificial water oxidation and dye degradation with silver phosphates: multi-faceted morphology matters, New J. Chem. 38 (2014) 1942–1945.
[29] S.B. Rawal, S. Do Sung, W.I. Lee, Novel Ag_3PO_4/TiO_2 composites for efficient decomposition of gaseous 2-propanol under visible-light irradiation, Catal. Commun. 17 (2012) 131–135.
[30] Febiyanto, I.V. Eliani, A. Riapanitra, U. Sulaeman, Synthesis and visible light photocatalytic properties of iron oxide–silver orthophosphate composites, in: AIP Conference Proceedings, AIP Publishing, 2016, p. 020021.
[31] X. Lin, J. Hou, S. Jiang, Z. Lin, M. Wang, G. Che, A Z-scheme visible-light-driven $Ag/Ag_3PO_4/Bi_2MoO_6$ photocatalyst: synthesis and enhanced photocatalytic activity, RSC Adv. 5 (2015) 104815–104821.
[32] K. Huang, Y. Lv, W. Zhang, S. Sun, B. Yang, F. Chi, S. Ran, X. Liu, One-step synthesis of Ag_3PO_4/Ag photocatalyst with visible-light photocatalytic activity, Mater. Res. 18 (2015) 939–945.
[33] Y. Liu, L. Fang, H. Lu, L. Liu, H. Wang, C. Hu, Highly efficient and stable Ag/Ag_3PO_4 plasmonic photocatalyst in visible light, Catal. Commun. 17 (2012) 200–204.
[34] Y.-S. Xu, W.-D. Zhang, Monodispersed Ag_3PO_4 nanocrystals loaded on the surface of spherical Bi_2MoO_6 with enhanced photocatalytic performance, Dalton Trans. 42 (2013) 1094–1101.
[35] W. Yao, B. Zhang, C. Huang, C. Ma, X. Song, Q. Xu, Synthesis and characterization of high efficiency and stable Ag_3PO_4/TiO_2 visible light photocatalyst for the degradation of methylene blue and rhodamine B solutions, J. Mater. Chem. 22 (2012) 4050–4055.
[36] M.N. Shaddad, D. Cardenas-Morcoso, P. Arunachalam, M. Garcia-Tecedor, M.A. Ghanem, J. Bisquert, A. Al-Mayouf, S. Gimenez, J. Phys. Chem. C 122 (2018) 11608–11615.
[37] S. Bai, M. Cao, Y. Jin, X. Dai, X. Liang, Z. Ye, M. Li, J. Cheng, X. Xiao, Z. Wu, Low-temperature combustion-synthesized nickel oxide thin films as hole-transport interlayers for solution-processed optoelectronic devices, Adv. Energy Mater. 4 (2014) 1301460.
[38] W. Teng, X. Li, Q. Zhao, G. Chen, Fabrication of $Ag/Ag_3PO_4/TiO_2$ heterostructure photoelectrodes for efficient decomposition of 2-chlorophenol under visible light irradiation, J. Mater. Chem. A 1 (2013) 9060–9068.
[39] Z. Lei, J. Bai, Y. Li, Z. Wang, C. Zhao, Fabrication of nanoporous nickel-iron hydroxylphosphate composite as bifunctional and reversible catalyst for highly efficient intermittent water splitting, ACS Appl. Mater. Interfaces 9 (2017) 35837–35846.
[40] W. Bian, Y. Huang, X. Xu, M.A. Ud Din, G. Xie, X. Wang, Iron hydroxide-modified nickel hydroxylphosphate single-wall nanotubes as efficient electrocatalysts for oxygen evolution reactions, ACS Appl. Mater. Interfaces 10 (2018) 9407–9414.
[41] D. Kang, Y. Park, J.C. Hill, K.-S. Choi, Preparation of Bi-based ternary oxide photoanodes $BiVO_4$, Bi_2WO_6, and $Bi_2Mo_3O_{12}$ using dendritic Bi metal electrodes, J. Phys. Chem. Lett. 5 (2014) 2994–2999.
[42] M.N. Shaddad, M.A. Ghanem, A.M. Al-Mayouf, S. Giménez Juliá, J. Bisquert, I. Herraiz Cardona, Cooperative catalytic effect of ZrO_2 and a-Fe_2O_3 nanoparticles on $BiVO_4$ photoanodes for enhanced photoelectrochemical water splitting, ChemSusChem 9 (2016) 2779–2783.
[43] F. Chen, Q. Yang, X. Li, G. Zeng, D. Wang, C. Niu, J. Zhao, H. An, T. Xie, Y. Deng, Hierarchical assembly of graphene-bridged $Ag_3PO_4/Ag/BiVO_4$ (040) Z-scheme photocatalyst: an efficient, sustainable and heterogeneous catalyst with enhanced visible-light photoactivity towards tetracycline degradation under visible light irradiation, Appl. Catal. B 200 (2017) 330–342.
[44] C. Li, P. Zhang, R. Lv, J. Lu, T. Wang, S. Wang, H. Wang, J. Gong, Selective deposition of Ag_3PO_4 on monoclinic $BiVO_4$ (0 4 0) for highly efficient photocatalysis, Small 9 (2013) 3951–3956.
[45] W. Teng, X. Li, Q. Zhao, J. Zhao, D. Zhang, In situ capture of active species and oxidation mechanism of RhB and MB dyes over sunlight-driven Ag/Ag_3PO_4 plasmonic nanocatalyst, Appl. Catal. B 125 (2012) 538–545.
[46] S.Y. Jeong, H.-M. Shin, Y.-R. Jo, Y.J. Kim, S. Kim, W.-J. Lee, G.J. Lee, J. Song, B.J. Moon, S. Seo, Plasmonic silver nanoparticle-impregnated nanocomposite $BiVO_4$ photoanode for plasmon-enhanced photocatalytic water splitting, J. Phys. Chem. C 122 (2018) 7088–7093.
[47] J. Zhang, Y. Yang, Z. Zhang, X. Xu, X. Wang, Rapid synthesis of mesoporous Ni_xCo_{3-x} $(PO_4)_2$ hollow shells showing enhanced electrocatalytic and supercapacitor performance, J. Mater. Chem. A 2 (2014) 20182–20188.
[48] S. Li, Y. Wang, S. Peng, L. Zhang, A.M. Al-Enizi, H. Zhang, X. Sun, G. Zheng, Co–Ni-based nanotubes/nanosheets as efficient water splitting electrocatalysts, Adv. Energy Mater. 6 (2016) 1501661.
[49] X. Yang, H. Tang, J. Xu, M. Antonietti, M. Shalom, Silver phosphate/graphitic carbon nitride as an efficient photocatalytic tandem system for oxygen evolution, ChemSusChem 8 (2015) 1350–1358.
[50] J.-W. Xu, Z.-D. Gao, K. Han, Y. Liu, Y.-Y. Song, Synthesis of magnetically separable $Ag_3PO_4/TiO_2/Fe_3O_4$ heterostructure with enhanced photocatalytic performance under visible light for photoinactivation of bacteria, ACS Appl. Mater. Interfaces 6 (2014) 15122–15131.